

Maximized electron interactions at the magic angle in twisted bilayer graphene

Alexander Kerelsky¹, Leo J. McGilly¹, Dante M. Kennes², Lede Xian³, Matthew Yankowitz¹, Shaowen Chen^{1,4}, K. Watanabe⁵, T. Taniguchi⁵, James Hone⁶, Cory Dean¹, Angel Rubio^{3,7*} & Abhay N. Pasupathy^{1*}

The electronic properties of heterostructures of atomically thin van der Waals crystals can be modified substantially by moiré superlattice potentials from an interlayer twist between crystals^{1,2}. Moiré tuning of the band structure has led to the recent discovery of superconductivity^{3,4} and correlated insulating phases⁵ in twisted bilayer graphene (TBG) near the ‘magic angle’ of twist of about 1.1 degrees, with a phase diagram reminiscent of high-temperature superconductors. Here we directly map the atomic-scale structural and electronic properties of TBG near the magic angle using scanning tunnelling microscopy and spectroscopy. We observe two distinct van Hove singularities (VHSs) in the local density of states around the magic angle, with an energy separation of 57 millielectronvolts that drops to 40 millielectronvolts with high electron/hole doping. Unexpectedly, the VHS energy separation continues to decrease with decreasing twist angle, with a lowest value of 7 to 13 millielectronvolts at a magic angle of 0.79 degrees. More crucial to the correlated behaviour of this material, we find that at the magic angle, the ratio of the Coulomb interaction to the bandwidth of each individual VHS (U/t) is maximized, which is optimal for electronic Cooper pairing mechanisms. When doped near the half-moiré-band filling, a correlation-induced gap splits the conduction VHS with a maximum size of 6.5 millielectronvolts at 1.15 degrees, dropping to 4 millielectronvolts at 0.79 degrees. We capture the doping-dependent and angle-dependent spectroscopy results using a Hartree–Fock model, which allows us to extract the on-site and nearest-neighbour Coulomb interactions. This analysis yields a U/t of order unity indicating that magic-angle TBG is moderately correlated. In addition, scanning tunnelling spectroscopy maps reveal an energy- and doping-dependent three-fold rotational-symmetry breaking of the local density of states in TBG, with the strongest symmetry breaking near the Fermi level and further enhanced when doped to the correlated gap regime. This indicates the presence of a strong electronic nematic susceptibility or even nematic order in TBG in regions of the phase diagram where superconductivity is observed.

Van der Waals heterostructures of atomically thin layers with a rotational misalignment yield a structural moiré superlattice, often inducing new electronic properties^{2,6,7}. TBG is a particularly interesting case in which the band structure has two VHSs with energy separation determined by the moiré period² and interlayer hybridization^{8–11}. A continuum model analysis¹ of the band structure of TBG predicted that near 1.1°, which is a ‘magic angle’, the separation tends to zero, creating a two-dimensional region in momentum space where the states have almost no dispersion. The low-energy physics of the electrons would then be largely determined by the Coulomb interaction and lead to the possibility of emergent many-body ground states⁶. Indeed, recent transport measurements have shown the presence of both superconducting^{3,4} and insulating states⁵ under these conditions. The phase diagram is reminiscent of unconventional superconductors,

but in a two-dimensional, gate-tunable material with simple chemistry. These developments establish TBG as a model system in which bandwidth and interactions can be tuned using simple experimental knobs (changing the electrostatic gate voltage with a power supply can sweep both carrier density and displacement field within one device, which modifies bandwidth and interactions), thus paving the way towards understanding unconventional superconductivity.

Despite rapid progress, the precise experimental atomic and electronic structure of TBG at the magic angle is unknown. This has posed a challenge for theoretical modelling—in particular, theory has not established the origin of the correlated insulating phases^{12–16} or whether the superconducting pairing is mediated by electronic interactions. Therefore, direct measurements of the atomic and low-energy electronic structure are required. Here we present measurements of the local angle- and doping-dependent atomic-scale structure and the local density of states (LDOS) of near-magic-angle TBG on hexagonal boron nitride (hBN) using scanning tunnelling microscopy (STM) and scanning tunnelling spectroscopy (STS) at 5.7 K. Although previous STM works have explored TBG, measurements were at angles far from the magic angle^{8,17}, or on conducting substrates where electrostatic doping is not possible and the Coulomb interaction is screened^{9–11}. Our samples are nominally similar to transport devices in which superconductivity has been measured, although our samples do not have a top hBN layer in order to access the bilayer graphene with the STM tip.

An optical image and schematic of a typical sample are shown in Fig. 1a, b. Figure 1c shows the structure of a TBG moiré. Within a moiré unit cell, the two layer atomic stacking arrangement displays regions of AA, AB/BA (Bernal) and saddle-point stacking^{17,18}. Figure 1d–f shows typical atomic-resolution topographic images of TBG at various small angles. The bright spots are the AA sites, while the dark regions are the AB/BA sites^{8,17}. No TBG-hBN moiré pattern is present because we have intentionally made the TBG-hBN angle large to minimize the hBN interaction. Without strain and disorder, a single moiré wavelength exists which can be used to determine the twist angle. In our samples and previous spatial studies, a small amount of heterostrain is present (arising in the conventional fabrication method) yielding a different moiré period along the principal directions of the moiré lattice. We use a comprehensive model (Supplementary Information section S1) to extract the precise local twist angle and strain, finding uniaxial strain between 0.1% and 0.7% at these small twist angles. Variability in strain or twist probably causes variable transport results, even within different regions of a single device⁴.

One important structural consideration in TBG is the nature of the saddle-point region at the AB/BA interface. At large twist angles ($>4^\circ$), the superlattice structure evolves smoothly, whereas at small angles ($<0.5^\circ$), AB/BA regions are maximized, producing topological domain walls at the saddle-point regions^{17,18}. The magic angle is in an intermediate regime. Domain-wall-like lines are to some degree visible in all three angles in Fig. 1d–f. Figure 1g shows normalized

¹Department of Physics, Columbia University, New York, NY, USA. ²Dahlem Center for Complex Quantum Systems and Fachbereich Physik, Freie Universität Berlin, Berlin, Germany. ³Max Planck Institute for the Structure and Dynamics of Matter, Hamburg, Germany. ⁴Department of Applied Physics and Applied Mathematics, Columbia University, New York, NY, USA. ⁵National Institute for Materials Science, Tsukuba, Japan. ⁶Department of Mechanical Engineering, Columbia University, New York, NY, USA. ⁷Center for Computational Quantum Physics, The Flatiron Institute, New York, NY, USA. *e-mail: angel.rubio@mpsd.mpg.de; apn2108@columbia.edu

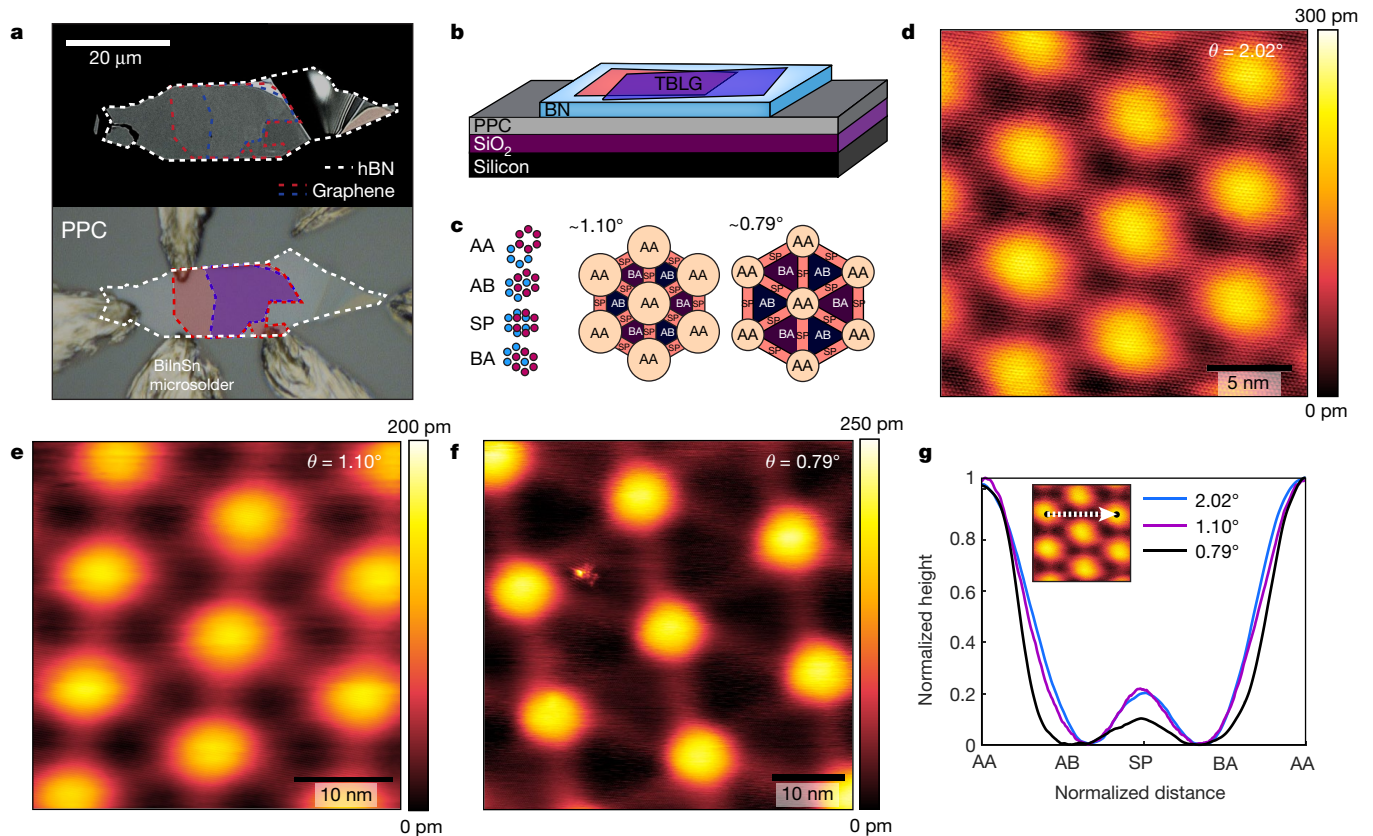


Fig. 1 | Atomic insights on TBG structure near the magic angle.

a, Optical images of one of the measured samples. Dashed lines highlight the layers of hBN and the two twisted monolayers of graphene. The top is mid-fabrication, immediately after stacking, and the bottom is the final structure contacted (using the microsoldering technique described in Methods) with bismuth indium tin (BiInSn) on polypropylene carbonate (PPC). **b**, Sample schematic. **c**, Schematics of a real-space moiré pattern

interchanging between AA, AB/BA and saddle-point (SP) stacking.

d–f, Atomic-resolution STM topographies on 2.02°, 1.10° and 0.79° TBG samples. Topographies were taken at 1 V and 50 pA, at 0.5 V and 30 pA, and at 0.5 V and 50 pA, respectively. **g**, Normalized spatial height profiles from the AA site to the second-nearest AA site, as delineated in the inset, for the three twist angles shown in **d–f**.

height profiles along the direction of the next-nearest neighbour AA (dotted line in Fig. 1g) for the three angles, allowing direct comparison of the extent of each stacking arrangement (see Supplementary Information section S2 for bias dependence). We find that atomic rearrangements towards domain-wall saddle-point regions are important at all of these small angles, including 1.10°, which will be relevant to future theoretical modelling (for instance, it is predicted that this reconstruction suppresses other magic angles¹⁹).

Figure 2a shows STS measurements of the LDOS on the AA stacked regions for a series of small twist angles (3.49° to 0.79°) at zero external doping. The LDOS profiles show a filled (valence) and an unfilled (conduction) VHS (black arrows). The VHSs shift in energy towards the Dirac point with decreasing twist angle, as previously shown⁸. Figure 2d shows the VHS separation angle dependence. At 1.10°, where superconductivity is observed, there are still two distinct peaks in the LDOS separated by about 57 ± 2 meV. At the smallest angle studied here, 0.79°, the VHSs nearly merge, with a separation of 13 ± 2 meV.

We compare the experimental spectra to tight-binding calculations (see Methods). We note that we use an intralayer hopping fitted to the experimental Fermi velocity for monolayer graphene, unlike previous work^{10,20} that used density functional theory monolayer band structures (which underestimate the Fermi velocity by about 20%, a many-body correlation effect that can be corrected using many-body GW self-energy calculations²¹; see Supplementary Information section S3). Figure 2b shows the results for angles of 1.10° and larger, matching the experimental VHS separations well, as plotted in Fig. 2d. At 1.10°, the VHS separation calculated by our tight-binding model is about 41 meV, comparable with the 57-meV STS value, but much larger than for other

tight-binding models of TBG near 1.10° (less than 5 meV)^{3,22}. The larger intralayer hopping in our tight-binding model implies that the Fermi velocity vanishes at a smaller angle than previously reported²². We have considered other experimental effects that can affect the measured VHS separation and do not believe that they contribute substantially (Supplementary Information section S4).

Figure 2c shows higher-resolution STS LDOS profiles at 0.79° versus the magic angle. Although the peaks at 0.79° are closer together than at 1.15°, the individual VHS width is not smaller. Extraction of the valence half-width reveals 10 ± 1 meV at 1.15° and 11 ± 1 meV at 0.79°. Extraction of the conduction half-width reveals 13 ± 1 meV at 1.15° and 13 ± 1 meV at 0.79° (the conduction half-widths drop to 9.5 ± 1 and 10 ± 1 meV when doped near the Fermi level; Extended Data Fig. 1f). Figure 2e shows the angle-dependent half-widths of the valence and conduction VHS peaks at zero external doping. The average peak half-widths gradually decrease with decreasing angle (about 30 meV per degree) at angles above 1.5°. The width then sharply drops to about 10 meV at the magic angle. The importance of electron correlations is determined by the ratio of on-site Coulomb interaction, U , to bandwidth, t , of an electron in a single VHS band (that is isolated from other bands). Following simple geometric principles, U decreases proportionally to $1/\lambda$, where λ is the moiré wavelength. Our angle-dependent measurements of bandwidth t therefore imply that the ratio U/t is maximum at the magic angle, and superconductivity arises in a single isolated VHS band^{13,16} with maximized electron correlations. We also note that the conduction VHS is wider at all angles, indicating band structure electron–hole asymmetry consistent with recent calculations¹⁹.

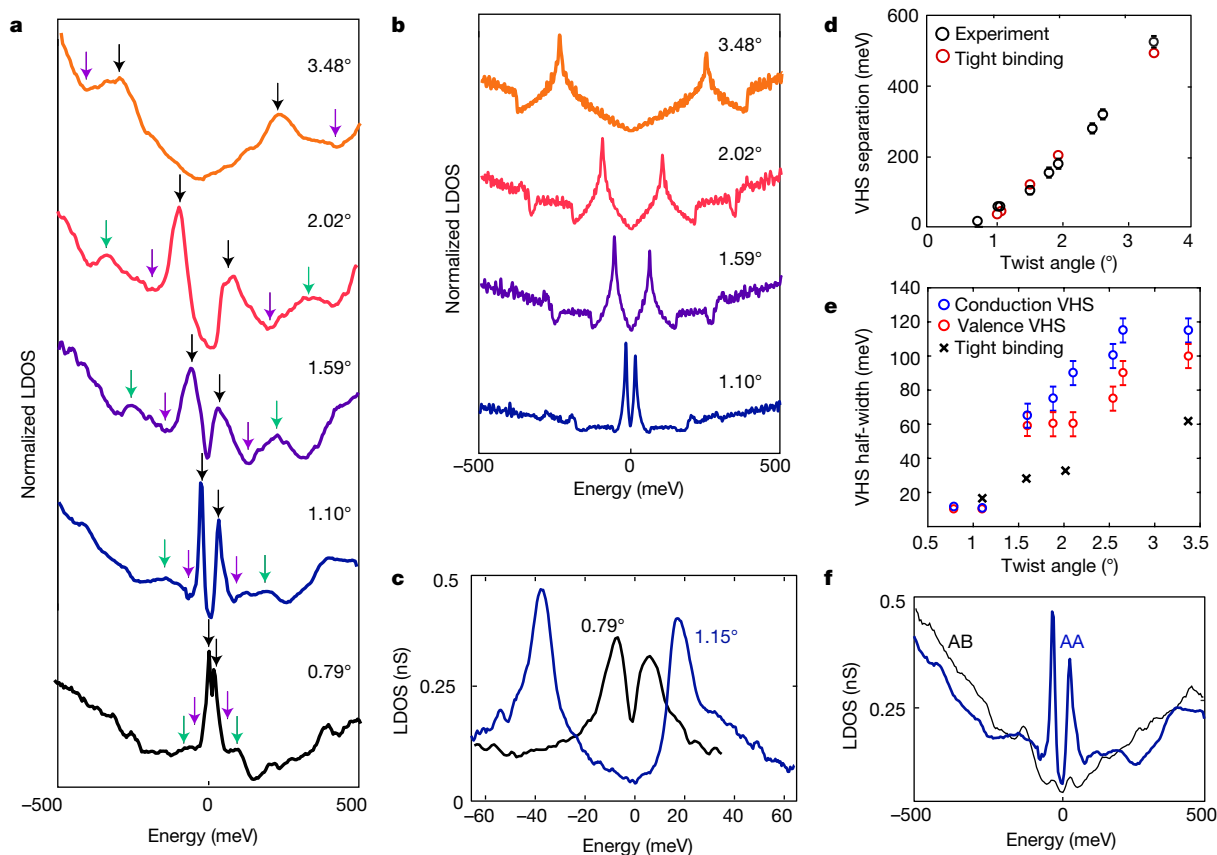


Fig. 2 | LDOS and bandwidth of TBG at the magic angle. **a**, STS LDOS at zero external doping on moiré AA sites of 3.48°, 2.02°, 1.59°, 1.10° and 0.79°, normalized to the maximum value for each curve and vertically offset for clarity. Arrows show several prominent features consistent at all angles—the VHSs (black arrows), the first dips (purple arrows) and a second smaller peak (green arrows) previously observed. With decreasing twist angle, all features shift towards the Fermi level. **b**, Tight-binding calculations of the LDOS at the measured angles down to 1.10°. **c**, High-energy-resolution zoom-in of STS LDOS on 1.15° and 0.79° AA sites.

Measurements are taken in a closed loop at the 100-meV and 50-pA setpoints with a 0.5-meV and 1-meV oscillation. **d**, Experimental versus tight-binding VHS separation as a function of twist angle. **e**, Experimental conduction and valence VHS half-widths versus tight-binding half-widths as a function of twist angle. **f**, STS LDOS on AA versus AB sites in 1.10° TBG. Error bars in **d** and **e** are derived from the sum of squares of the lock-in oscillation used to identify features (0.5 meV for near-magic angle, 1 meV for 0.79° and 10 meV for 1.5° and above).

We now turn to the doping-dependent AA site LDOS. Figure 3a, b shows spectra as a function of back-gate voltage on two TBG samples at 1.10° and 1.15°, limited in gate voltage by gate leakage (see Methods). The positions, shapes and separation of the VHSs are a sensitive function of doping. In the 1.15° sweep (Fig. 3b) we were able to dope past electron half-filling of the moiré superlattice, $-0.5n_s$ (n_s is four carriers per moiré unit cell), which was not possible in the 1.10° sample. A finer set of doping-dependent spectra around electron half-filling is shown in Fig. 3c. As the conduction VHS peak is crossing the Fermi level, it splits and a gap emerges that is maximized at a doping of about $-1.5 \times 10^{12} \text{ cm}^{-2}$ (magenta in Fig. 3d). The gap persists for a doping range of $2 \times 10^{11} \text{ cm}^{-2}$ with a peak-to-peak value of $6.5 \pm 0.5 \text{ meV}$. In transport, the largest gap is observed at half-filling of the moiré conduction band. Based on our moiré unit cell area, this corresponds to a doping of $-1.55 \times 10^{12} \text{ cm}^{-2}$, within the error of the spectroscopy gap doping. The persistence of the gap for $2 \times 10^{11} \text{ cm}^{-2}$ is also consistent with the half-filling insulator doping range in transport. Thus, this gap is naturally associated with the correlated insulator state. The magnitude of the spectroscopy gap, however, is much bigger than the activation energy of the resistance in transport measurements, probably owing to disorder averaging, which always produces smaller activation gaps in transport than spectroscopy²³.

One important question that we can address is whether the gap opens precisely at the VHS peak or simply at a moiré lattice commensurate filling. To quantitatively investigate this, we integrate the LDOS over a small range (1.5 meV) on the electron-versus-hole side

of the Fermi level at each doping. The integrated LDOS profiles are plotted in Fig. 3e. The dip in the profiles corresponds to the correlated gap, which is maximized when the two curves cross within the dip at $-1.5 \times 10^{12} \text{ cm}^{-2}$ (about $0.5n_s$). The highest integrated LDOS where the curves cross, $-1.87 \times 10^{12} \text{ cm}^{-2}$ (about $0.6n_s$), corresponds to the VHS peak precisely at the Fermi level. Figure 3d shows the spectra at these two dopings. The analysis reveals that the gap opens on the shoulder of the VHS rather than the peak. Such a gap is more consistent with a Mott insulator, which occurs at commensurate filling, rather than a density wave order, which more naturally occurs at a density of states peak. This also provides band structure explanations for the extreme anisotropies seen in transport²⁴ on either side of half-filling, where the temperature-dependent resistance, effective mass and Hall coefficient are strongly asymmetric. Interestingly, we note that the doping difference between the maximized correlated gap and the VHS peak at the Fermi level is the same as the doping difference between the half-filling correlated insulator state and the highest-transition-temperature superconducting dome in transport. In transport, additional gaps emerge at quarter and three-quarter filling of the moiré bands^{4,5}. We have not seen these, possibly owing to the measurement temperature.

Next, we discuss the separation between the two VHSs, which is maximum at charge neutrality and reduced with electron/hole doping. This behaviour is reminiscent of the quasiparticle gap in two-dimensional semiconductors with doping. We model this with a simple one-band model on a honeycomb lattice with nearest-neighbour

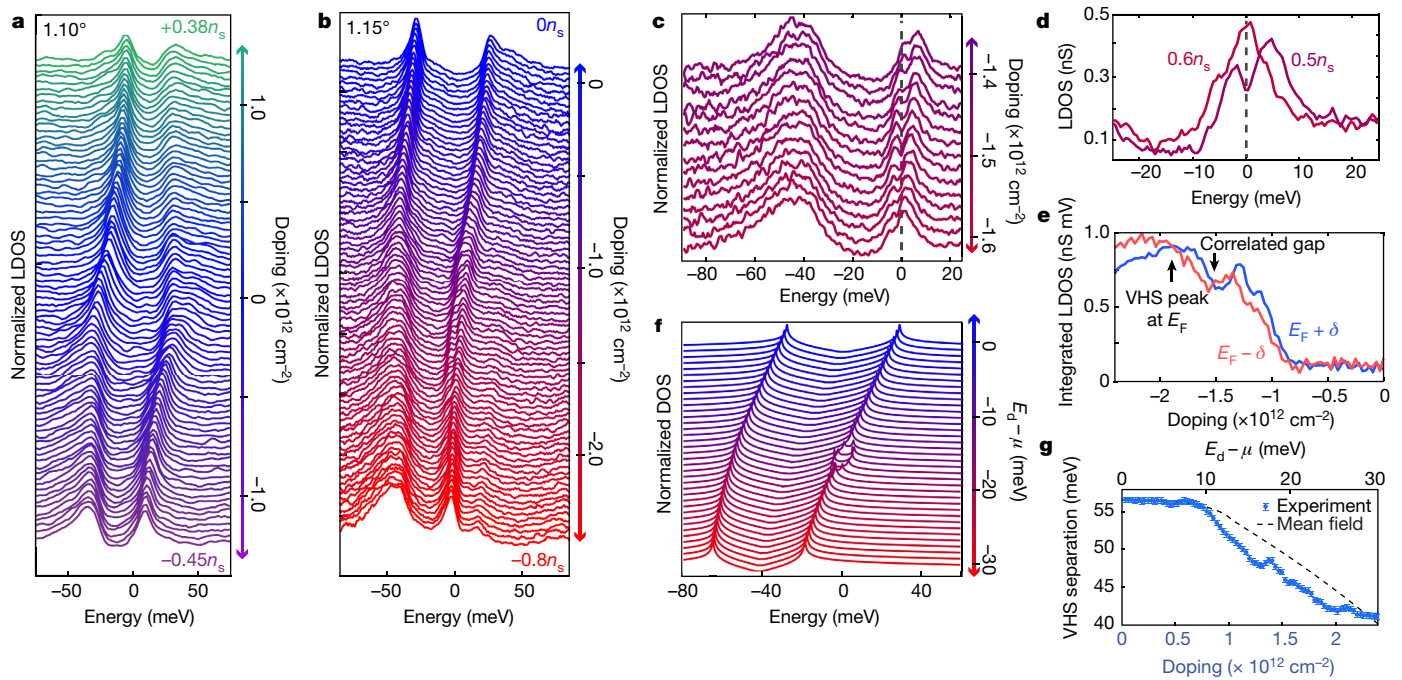


Fig. 3 | Doping dependence of magic-angle LDOS peaks. **a, b**, STS LDOS on a 1.10° AA site (**a**) and a 1.15° AA site (**b**) as a function of doping. Curves are offset for clarity. Doping is given in units of cm^{-2} and fractional filling of the moiré superlattice with four electrons or holes (n_s). In **a**, spectra were taken in a closed loop at 200-meV and 50-pA setpoints with an oscillation of 1 meV for 1.10°. In **b**, spectra were taken in a closed loop at 100-meV and 50-pA setpoints with an oscillation of 0.5 meV for 1.15°. **c**, Zoom-in to **b** around half-filling of the moiré superlattice ($-0.5n_s$), revealing a gap as the VHS crosses the Fermi level E_F . **d**, Zoom-in of the conduction VHS at $-1.5 \times 10^{12} \text{ cm}^{-2}$ ($-0.6n_s$) (magenta) and

$-1.87 \times 10^{12} \text{ cm}^{-2}$ ($-0.6n_s$) (red), where the gap is most prominent and the VHS peak is at E_F , respectively. **e**, Integrated LDOS from E_F to $\delta = 1.5 \text{ meV}$ below and above the Fermi level, showing the crossings where the gap is maximized and where the VHS peak is at the Fermi level, as highlighted in **d**. **f**, Hartree-Fock mean-field density of states, offset as a function of chemical potential shift from neutrality, $E_d - \mu$. **g**, Experimental VHS separation versus doping and mean-field VHS separation versus chemical potential ($E_d - \mu$). The uncertainty is derived from the sum of squares of the lock-in oscillation used to identify features.

hopping $t_0 = 16.3 \text{ meV}$. We include correlations via on-site and nearest-neighbour repulsive interactions U and V_1 , respectively, and study the spectrum of the system in the Hartree-Fock approximation (Supplementary Information section S5). The results are shown in Fig. 3f. The nearest-neighbour interaction V_1 renormalizes the hopping via its Fock contribution, causing a doping-dependent VHS separation. $V_1 = 6.26 \text{ meV}$ best reproduces the experimental dependence of VHS separation, as shown in Fig. 3g, plotting theoretical separation as a function of chemical potential and experimental separation as a function of doping. Theory captures the relatively doping-independent separation near charge neutrality and the strong decrease with higher doping. In this simple model, the on-site interaction U opens a gap at half-filling owing to Fermi surface nesting. Although this level of theory is inadequate to determine the true nature of the gap, we use it as a simple way to quantify the on-site U . $U = 4.03 \text{ meV}$ approximately reproduces the STS gap, showing that magic-angle TBG is a moderately correlated material with U/t of order unity. The peak shapes in Fig. 3a, b also display interesting doping dependence: when doped near the Fermi level, they sharpen, whereas when doped away from the Fermi level, they become highly asymmetric (quantified for the valence VHS in Extended Data Fig. 2). This is characteristic of spectroscopy on strongly correlated materials^{25–27} (see Supplementary Information section S6 for further discussion).

A natural question is how the correlated gap evolves with angle. We present doping-dependent LDOS of the 0.79° TBG in Extended Data Fig. 1. Most of the observed phenomenology is the same as at the magic angle: changing VHS shapes, separation and a gap emerging around electron half-filling. Compared to the correlated gap at the magic angle, the half-filling gap at 0.79° is less pronounced and smaller, being $4 \pm 1 \text{ meV}$ as opposed to $6.5 \pm 1 \text{ meV}$ observed at 1.15°. This corroborates that correlation effects are reduced at 0.79° (see Supplementary Information section S7 for further discussion).

Next we turn to the LDOS spatial dependence in magic-angle TBG. Figure 4a shows an STS map energy slice at the conduction VHS peak (zero external doping) of one moiré cell at 1.15°. When undoped, LDOS maps at energies around the VHS peaks show the same contrast as the topographies. For comparison, the tight-binding probability density (see Methods) of a single wavefunction at this energy is plotted in Fig. 4b. We compare line profiles of the experimental and tight-binding LDOS in Fig. 4c. The tight-binding wavefunction systematically underestimates the saddle-point region intensity and is more confined around the AA site than in the experiment, something to consider in future calculations.

Finally, we focus on the doping- and energy-dependent STS maps. In a perfect moiré lattice at the single particle level, the LDOS should have three-fold (C_3) rotational symmetry. The small amount of strain present, however, introduces some symmetry breaking. We explore whether this symmetry breaking is uniform with energy and doping (which could be trivially due to the strain), or is enhanced at certain energies^{28,29} and dopings. To quantify the energy-dependent anisotropy, we use a technique shown in Fig. 4d (described in Methods). Energy-dependent anisotropies for three dopings below half-filling are plotted in Fig. 4e with AA site LDOS averages from the corresponding maps. The energy-dependent anisotropy is not uniform; however, despite large asymmetries at other energies, at around the conduction VHS the LDOS is symmetric at these dopings. This is visualized in the map slices at the conduction VHS peak and $\pm 5 \text{ meV}$ around it, shown in the top three rows of Fig. 4g. This is in stark contrast to Fig. 4f at half-filling in doping when the correlated gap emerges. In this situation, the anisotropy is highly enhanced at energies around the gap, visualized in the bottom row of Fig. 4g, showing the map slices at and around the correlated gap. The LDOS strongly breaks three-fold (C_3) symmetry around the correlated gap, where the wavefunction was symmetric at lower dopings. Additionally, the symmetry breaking at all dopings is

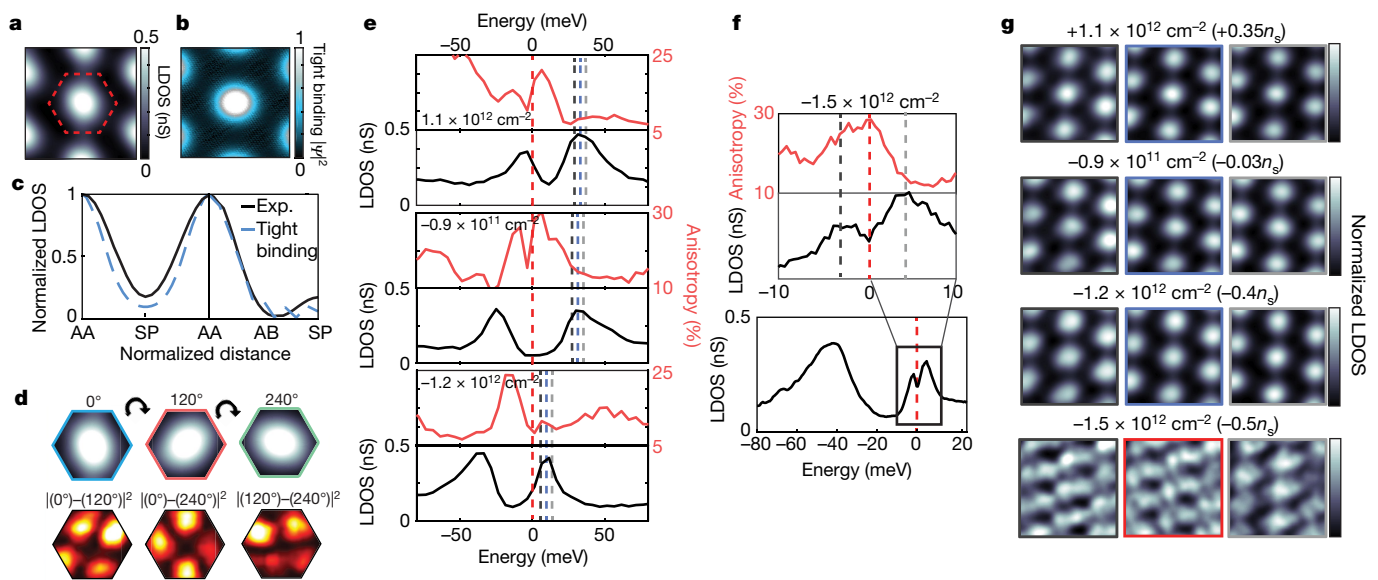


Fig. 4 | Wavefunctions and symmetry breaking in magic-angle TBG under doping. **a**, STS LDOS spatial map at 50 meV above the E_F value of a moiré cell (centred at AA) in zero externally doped 1.15° TBG. **b**, Probability density distribution of a single K-point wavefunction Ψ , calculated using tight binding. **c**, Spatial line cuts comparing the experimental/tight-binding LDOS in the nearest and second-nearest AA directions. **d**, Procedure for quantifying anisotropy, as outlined in the text. The top row shows the three rotations of an isolated AA site Wigner-Seitz cell and the bottom row shows the three combinations of the magnitude of the difference between the cells. **e**, Averaged STS map AA site LDOS profiles and their anisotropy as a function of energy for three dopings below half electron or hole filling ($\pm 0.5n_s$). Dashed lines correspond to the Fermi level, the conduction VHS peak and ± 5 meV around the

conduction VHS peak for each doping in the first three rows of **g**. **f**, Averaged STS map AA site LDOS at half electron filling ($-0.5n_s$), around the correlated gap, and the associated enhanced anisotropy. Dashed lines correspond to the newly split peaks and the correlated gap (-3 meV, Fermi level, 4 meV), which are spatially plotted in the bottom row of **g**. **g**, STS spatial images corresponding to the dopings and dashed lines in **e** and **f**. The first three rows are at dopings below half-filling, as indicated, and at energies 5 meV below the conduction VHS peak, at the conduction VHS peak and 5 meV above the conduction VHS peak. The final row is at half electron filling, at energies 3 meV below the correlated gap (lower split peak), in the correlated gap (Fermi level) and 4 meV above the correlated gap (higher split peak), as shown by the dashed lines in **f**.

strongest in a narrow region of energy around the Fermi level, as evidenced by the anisotropy peaks in Fig. 4e, f, which shift with doping (full spatial slices are shown in Supplementary Information section S8). These findings indicate that the electronic structure is nematic, with the strongest nematicity near half-filling. Two possibilities exist to explain the observed nematicity: (1) it is possible that the electronic structure has a strong nematic susceptibility and strain breaks the three-fold (C3) symmetry allowing visualization of the nematic susceptibility, as recently observed in the iron pnictides in the high-temperature tetragonal phase^{28,30}; and (2) it is possible that a true nematic order exists, independent of strain. In this scenario, we would expect domains of nematic order with different orientation, which we have not observed so far. Future measurements should focus on this, because our samples were not uniform over large enough areas to test for this (Supplementary Information section S9). Whether a translational symmetry breaking occurs simultaneously (that is, by Fermi surface nesting³¹; see Supplementary Information section S10) is also unclear.

Our spectroscopic measurements of magic-angle TBG provide insights into the nature of the superconducting and insulating states seen in transport. The VHS separation is larger than previously thought around 1.1° , implying that the physics of correlated states is to be understood in the context of doping through a single VHS. Regarding superconducting order, electronic pairing mechanisms such as spin fluctuations are expected to be important when the ratio of the on-site Coulomb interaction U to the bandwidth t is large. On the other hand, in phonon-mediated pairing scenarios, the superconducting transition temperature is improved by lowering the Coulomb pseudopotential (proportional to U) and increasing the density of states at the Fermi level. Our spectroscopic results show that U/t is maximized near 1.1° . Superconductivity in TBG is thus observed where $J = U^2/t$ is maximized, conditions that maximize electronic rather than phonon-based pairing. The insulating gap that emerges at half-filling of magic-angle TBG is not

at the peak of the VHS, and is therefore more consistent with a Mott insulator rather than a density wave picture. Our observation of energy- and doping-dependent symmetry breaking, maximized near the correlated gap at half-filling, is indicative of a strong nematic electronic susceptibility or order in magic-angle TBG. The interaction of such ordered states with superconductivity in TBG remains to be investigated.

Online content

Any methods, additional references, Nature Research reporting summaries, source data, extended data, supplementary information, acknowledgements, peer review information; details of author contributions and competing interests; and statements of data and code availability are available at <https://doi.org/10.1038/s41586-019-1431-9>.

Received: 23 December 2018; Accepted: 14 June 2019;

Published online 31 July 2019.

- Bistritzer, R. & MacDonald, A. H. Moiré bands in twisted double-layer graphene. *Proc. Natl Acad. Sci. USA* **108**, 12233–12237 (2011).
- Lopes dos Santos, J. M. B., Peres, N. M. R. & Castro Neto, A. H. Graphene bilayer with a twist: electronic structure. *Phys. Rev. Lett.* **99**, 256802 (2007).
- Cao, Y. et al. Unconventional superconductivity in magic-angle graphene superlattices. *Nature* **556**, 43–50 (2018).
- Yankowitz, M. et al. Tuning superconductivity in twisted bilayer graphene. *Science* **363**, 1059–1064 (2019).
- Cao, Y. et al. Correlated insulator behaviour at half-filling in magic-angle graphene superlattices. *Nature* **556**, 80–84 (2018).
- Wu, F., Lovorn, T., Tutuc, E. & MacDonald, A. H. Hubbard model physics in transition metal dichalcogenide moiré bands. *Phys. Rev. Lett.* **121**, 026402 (2018).
- Xian, L., Kennes, D. M., Tancogne-Dejean, N., Altarelli, M. & Rubio, A. Multi-flat bands and strong correlations in twisted bilayer boron nitride. Preprint at <https://arxiv.org/abs/1812.08097> (2018).
- Wong, D. et al. Local spectroscopy of moiré-induced electronic structure in gate-tunable twisted bilayer graphene. *Phys. Rev. B* **92**, 155409 (2015).
- Li, G. et al. Observation of Van Hove singularities in twisted graphene layers. *Nat. Phys.* **6**, 109–113 (2010).

10. Brihuega, I. et al. Unraveling the intrinsic and robust nature of van Hove singularities in twisted bilayer graphene by scanning tunneling microscopy and theoretical analysis. *Phys. Rev. Lett.* **109**, 196802 (2012).
11. Yin, L.-J., Qiao, J.-B., Zuo, W.-J., Li, W.-T. & He, L. Experimental evidence for non-Abelian gauge potentials in twisted graphene bilayers. *Phys. Rev. B* **92**, 081406 (2015).
12. Yuan, N. F. Q. & Fu, L. Model for the metal-insulator transition in graphene superlattices and beyond. *Phys. Rev. B* **98**, 045103 (2018).
13. Po, H. C., Zou, L. J., Vishwanath, A. & Senthil, T. Origin of Mott insulating behavior and superconductivity in twisted bilayer graphene. *Phys. Rev. X* **8**, 031089 (2018).
14. Padhi, B., Setty, C. & Phillips, P. W. Doped twisted bilayer graphene near magic angles: proximity to Wigner crystallization, not Mott insulation. *Nano Lett.* **18**, 6175–6180 (2018).
15. Isobe, H., Yuan, N. F. Q. & Fu, L. Unconventional superconductivity and density waves in twisted bilayer graphene. Preprint at <https://arxiv.org/abs/1805.06449> (2018).
16. Kennes, D. M., Lischner, J. & Karrasch, C. Strong correlations and d+id superconductivity in twisted bilayer graphene. Preprint at <https://arxiv.org/abs/1805.06310> (2018).
17. Huang, S. et al. Topologically protected helical states in minimally twisted bilayer graphene. *Phys. Rev. Lett.* **121**, 037702 (2018).
18. Yoo, H. et al. Atomic and electronic reconstruction at van der Waals interface in twisted bilayer graphene. Preprint at <https://arxiv.org/abs/1804.03806> (2018).
19. Carr, S., Fang, S., Zhu, Z. & Kaxiras, E. An exact continuum model for low-energy electronic states of twisted bilayer graphene. Preprint at <https://arxiv.org/abs/1901.03420> (2019).
20. Trambly de Laissardière, G., Mayou, D. & Magaud, L. Localization of Dirac electrons in rotated graphene bilayers. *Nano Lett.* **10**, 804–808 (2010).
21. Grüneis, A. et al. Electron-electron correlation in graphite: a combined angle-resolved photoemission and first-principles study. *Phys. Rev. Lett.* **100**, 037601 (2008).
22. Trambly de Laissardière, G., Mayou, D. & Magaud, L. Numerical studies of confined states in rotated bilayers of graphene. *Phys. Rev. B* **86**, 125413 (2012).
23. Xia, F., Farmer, D. B., Lin, Y.-m. & Avouris, P. Graphene field-effect transistors with high on/off current ratio and large transport band gap at room temperature. *Nano Lett.* **10**, 715–718 (2010).
24. Cao, Y. et al. Strange metal in magic-angle graphene with near Planckian dissipation. Preprint at <https://arxiv.org/abs/1901.03710> (2019).
25. Koralek, J. D. et al. Laser based angle-resolved photoemission, the sudden approximation, and quasiparticle-like spectral peaks in BSCCO. *Phys. Rev. Lett.* **96**, 017005 (2006).
26. Mo, S. K. et al. Prominent quasiparticle peak in the photoemission spectrum of the metallic phase of V_2O_3 . *Phys. Rev. Lett.* **90**, 186403 (2003).
27. Valla, T. et al. Coherence–incoherence and dimensional crossover in layered strongly correlated metals. *Nature* **417**, 627–630 (2002).
28. Rosenthal, E. P. et al. Visualization of electron nematicity and unidirectional antiferroic fluctuations at high temperatures in NaFeAs. *Nat. Phys.* **10**, 225–232 (2014).
29. Li, S.-Y. et al. Evidence of electron-electron interactions around Van Hove singularities of a graphene Moiré superlattice. Preprint at <https://arxiv.org/abs/1702.03501> (2017).
30. Andrade, E. F. et al. Visualizing the nonlinear coupling between strain and electronic nematicity in the iron pnictides by elasto-scanning tunneling spectroscopy. Preprint at <https://arxiv.org/abs/1812.05287> (2018).
31. Kim, Y. et al. Charge inversion and topological phase transition at a twist angle induced van Hove singularity of bilayer graphene. *Nano Lett.* **16**, 5053–5059 (2016).

Publisher's note: Springer Nature remains neutral with regard to jurisdictional claims in published maps and institutional affiliations.

© The Author(s), under exclusive licence to Springer Nature Limited 2019

METHODS

Experimental setup. Our fabrication of TBG samples followed the established ‘tearing’ method, using PPC as a polymer to sequentially pick up hBN, then half of a piece of graphene, followed by the second half but with a twist angle. This structure was flipped over and placed on an Si/SiO₂ chip. Direct contact was made to the TBG via microsoldering with Field’s metal³², keeping temperatures below 80 °C during the entire process to minimize the chance of layers rotating back to AB/BA stacking, which occurs when the structures are annealed.

Ultrahigh-vacuum STM/STS measurements were carried out in a home-built 5.7-K ultrahigh-vacuum STM. All tips used in this study were prepared on Au (111) and calibrated to be atomically sharp and to detect the Au (111) Shockley surface state via STS. Tens of freshly prepared tips were used in this study to ensure the consistency and accuracy of the findings.

Gate doping estimation. Owing to the PPC in our gate structure, we estimate gate-dependent carrier concentration by fabricating a parallel plate capacitor and measuring the capacitance per unit area in the STM at 5.7 K. All of our sample gating is limited to where gate leakage is below a nanoampere.

Anisotropy quantification technique. As shown in Fig. 4d, we begin by cropping to a single Wigner–Seitz cell of the triangular lattice formed by the LDOS in TBG. We affine-transform this cell to a perfect hexagonal shape to remove any effect of strain. Any breaking of three-fold (C₃) symmetry in the LDOS would imply that this cell is not symmetric under 120° and 240° degree rotations, as illustrated in Fig. 4d. We hence calculate the energy-dependent anisotropy:

$$A(E) = \frac{1}{3} \left(\frac{|I_{0^\circ}(E) - I_{120^\circ}(E)|}{n_{\text{pixel}}} + \frac{|I_{0^\circ}(E) - I_{240^\circ}(E)|}{n_{\text{pixel}}} + \frac{|I_{120^\circ}(E) - I_{240^\circ}(E)|}{n_{\text{pixel}}} \right),$$

where $I_{120^\circ}(E)$ and $I_{240^\circ}(E)$ refer to the spatial LDOS profiles of the 120°- and 240°-rotated Wigner–Seitz cells respectively and n_{pixel} is the number of pixels.

Tight-binding calculations. We model the twisted bilayer graphene system with the following tight-binding Hamiltonian²⁰:

$$H = \sum_{ij} t_{ij} |i\rangle \langle j|$$

where t_{ij} is the hopping parameter between p_z orbitals at the two lattice sites \mathbf{r}_i and \mathbf{r}_j , with the following form:

$$t_{ij} = (1 - n^2) \gamma_0 \exp \left[\lambda_1 \left(1 - \frac{|\mathbf{r}_i - \mathbf{r}_j|}{a} \right) \right] + n^2 \gamma_1 \exp \left[\lambda_2 \left(1 - \frac{|\mathbf{r}_i - \mathbf{r}_j|}{c} \right) \right]$$

where $a = 1.412 \text{ \AA}$ is the in-plane C–C bond length, $c = 3.36 \text{ \AA}$ is the interlayer separation, n is the direction cosine of $\mathbf{r}_i - \mathbf{r}_j$ along the out of plane axis (z axis), γ_0 (γ_1) is the intralayer (interlayer) hopping parameter, and λ_1 (λ_2) is the intralayer (interlayer) decay constant. This tight-binding model has been shown to reproduce the low-energy structure of TBG calculated by local density functional theory calculations with the following values for the parameters: $\gamma_0 = -2.7 \text{ eV}$, $\gamma_1 = 0.48 \text{ eV}$, $\lambda_1 = 3.15$ and $\lambda_2 = 7.50$. However, the Fermi velocity for monolayer graphene is usually 20% larger than what is calculated in density functional theory owing to correlation effects that are captured by GW calculations²¹. To incorporate those effects, we consider a larger intralayer hopping $\gamma_0' = 1.2\gamma_0$ (ref. ²¹) (the experimental parameter) as previously done^{8,10} (see Supplementary Information section S3).

For the calculation of LDOS, we employ the Lanczos recursive method³³ to calculate the LDOS in two twisted graphene sheets in real space with a system size larger than $200 \text{ nm} \times 200 \text{ nm}$ with an effective smearing of 1 meV. For the Hartree–Fock mean-field interactions model, see Supplementary Information section S5.

Data availability

The data presented in this work is available upon reasonable request to A.N.P.

Code availability

Code for the analysis described in Methods section ‘Anisotropy quantification technique’ and other analyses presented in this paper are available upon reasonable request.

32. Girit, Ç. Ö. & Zettl, A. Soldering to a single atomic layer. *Appl. Phys. Lett.* **91**, 193512 (2007).
33. Wang, Z. F., Liu, F. & Chou, M. Y. Fractal Landau-level spectra in twisted bilayer graphene. *Nano Lett.* **12**, 3833–3838 (2012).

Acknowledgements We thank A. Millis, J. Schmalian, L. Fu, R. Fernandes and S. Todadri for discussions. This work is supported by the Programmable Quantum Materials (Pro-QM) programme at Columbia University, an Energy Frontier Research Center established by the Department of Energy (grant DE-SC0019443). Equipment support is provided by the Office of Naval Research (grant N00014-17-1-2967) and Air Force Office of Scientific Research (grant FA9550-16-1-0601). Support for sample fabrication at Columbia University is provided by the NSF MRSEC programme through Columbia in the Center for Precision Assembly of Superstratic and Superatomic Solids (DMR-1420634). Theoretical work was supported by the European Research Council (ERC-2015-AdG694097). The Flatiron Institute is a division of the Simons Foundation. L.X. acknowledges the European Union’s Horizon 2020 research and innovation programme under the Marie Skłodowska-Curie grant agreement number 709382 (MODHET). A.N.P. and A.R. acknowledge support from the Max Planck—New York City Center for Non-Equilibrium Quantum Phenomena. D.M.K. acknowledges funding from the Deutsche Forschungsgemeinschaft through the Emmy Noether programme (KA 3360/2-1). C.D. acknowledges support by the Army Research Office under W911NF-17-1-0323 and The David and Lucile Packard foundation.

Author contributions A.K. performed STM measurements. L.J.M., M.Y. and S.C. fabricated samples for STM measurements. A.K. and L.J.M. performed experimental data analysis. K.W. and T.T. provided hBN crystals. D.M.K. and L.X. performed theoretical calculations. J.H., C.D., A.R. and A.N.P. advised. A.K. wrote the manuscript with assistance from all authors.

Competing interests : The authors declare no competing interests.

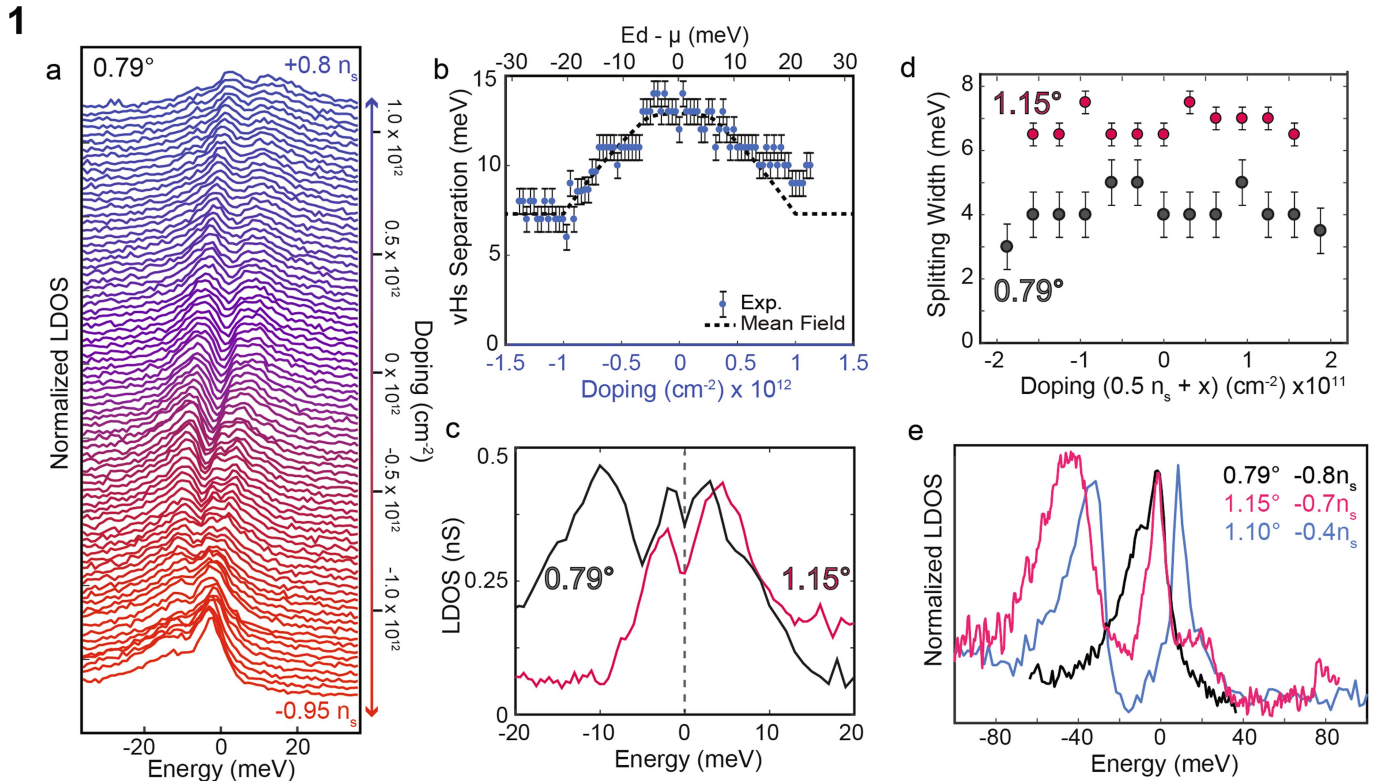
Additional information

Supplementary information is available for this paper at <https://doi.org/10.1038/s41586-019-1431-9>.

Correspondence and requests for materials should be addressed to A.R. or A.N.P.

Peer review information *Nature* thanks Miguel M. Ugeda and the other, anonymous, reviewer(s) for their contribution to the peer review of this work.

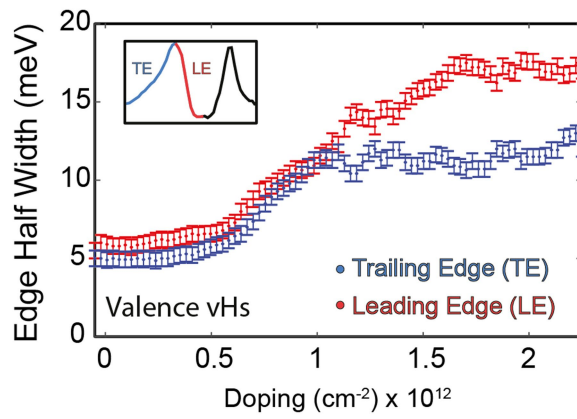
Reprints and permissions information is available at <http://www.nature.com/reprints>.



Extended Data Fig. 1 | 0.79° LDOS doping dependence. **a**, STS LDOS as a function of doping at a 0.79° TBG AA site for a doping range of $-0.95n_s$ to $0.8n_s$ (n_s being full filling of the moiré band with four electrons or holes). Spectra were taken in a closed loop at 100-meV and 50-pA setpoints with a 0.5-meV oscillation. **b**, Experimental VHS separation versus doping (bottom axis) and theoretical mean-field VHS separation as a function of chemical potential ($E_d - \mu$) relative to charge neutrality (top axis) for the 0.79° doping-dependent LDOS. **c**, LDOS comparison of the

correlated gap at half-filling ($-0.5n_s$) in 1.15° TBG and 0.79° TBG. **d**, Peak-to-peak gap size as a function of doping, offset to half-filling ($0.5n_s$) for 1.15° and 0.79° , where x is additional carrier doping in carriers per square centimetre around half-filling. **e**, Comparison of 0.79° , 1.15° and 1.10° LDOS when doped near the Fermi level, which is 0 V in the plot. The doping level of each curve is indicated in the legend. Error bars in **b** and **d** are estimated from the sum of squares of the lock-in oscillation (0.5 meV for 1.15° and 1 meV for 0.79°) used to determine feature positions.

2



Extended Data Fig. 2 | Asymmetry in valence VHS with doping. Half-widths of the trailing edge and leading edge of the valence VHS as a function of doping in the 1.15° sample. Error bars are estimated from the sum of squares of the lock-in oscillation (0.5 meV) used, which determines the peak half-width position.